REVIEW

Nanopillar photovoltaics: Materials, processes, and devices

Rehan Kapadia[a,b,c], Zhiyong Fan[a,b,c,1], Kuniharu Takei[a,b,c], Ali Javey[a,b,c,*]

[a]*Electrical Engineering and Computer Sciences, University of California, Berkeley, CA 94720, United States*
[b]*Berkeley Sensor and Actuator Center, University of California, Berkeley, CA 94720, United States*
[c]*Materials Sciences Division, Lawrence Berkeley National Laboratory, Berkeley, CA 94720, United States*

Abstract

Nanopillar photovoltaics present significant potential for fabrication of high-efficiency, low-cost solar cells. The advantages over planar cells, including wider materials choice, device geometries, and enhanced optical and electronic properties have been studied in detail over the past decade. Specifically, the 3-D geometry enables optimization of carrier collection and reduction of the material quality constraints. Furthermore, the anti-reflective and light trapping properties enable a drastic reduction in material necessary to absorb the majority of the incident light. Together, the optical and electronic advantages allow solar cell fabrication on low-cost substrates. However, the choice of the material system is important for taking advantage of the unique properties of nanopillar cells, especially given large surface/interface area. This review focuses on the recent work on the optical and electronic properties of nanopillar photovoltaics and the fabrication processes utilizing low-cost substrates.
© 2011 Elsevier Ltd. All rights reserved.

The main requirement for any competitive photovoltaic (PV) technology is the cost per watt installed. To achieve this goal, a PV technology must not only have a low unit area cost, but also high efficiency. Nanopillar (NPL) and nanowire (NW) PV [1–3] address these requirements in three ways: (i)

direct growth of crystalline materials on low-cost substrates without the use of complex epitaxial processes, (ii) maximization of carrier collection efficiency by decoupling the light absorption and carrier collection directions, and (iii) minimization of optical losses by reduced reflection and enhanced absorption. Significant work has been carried out in recent years on all aspects of NPL/NW photovoltaics including synthesis [4–7], optical properties [8–17], and device physics [18–22]. Additionally, both single NW devices [23–26] and arrays [13,27,28] have been studied in detail. Here, we review the recent work in our group and others on developing viable fabrication processes for NPL/NW PVs as

well as the optical and electronic properties of the resulting structures.

Of the possible architectures for NPL PVs, the two that enable enhanced carrier collection are NPLs embedded in a film [28] (Fig. 1a), and core-shell NPLs [29-31] (Fig. 1b). Considering these architectures, the optical and electronic design constraints on NPL PV are considerably relaxed compared to their planar counterparts. To prevent efficiency degradation through optical losses, the thickness of the cell must be greater than the absorption length of the material (Fig. 1c). Due to the excellent anti-reflective and light trapping properties of wire arrays [15,17], a significantly lower volume of active material, as compared to planar cells, can be used to absorb the majority of the incident solar photons. Similarly, by carefully tuning the geometry of the NPL cell, it is possible to maximize minority

Figure 1 Nanopillar architectures. (a) Array of NPLs embedded in a thin film; (b) NPL radial junctions; (c) schematic of a NPL PV cell with important lengths and recombination processes identified. Reprinted with permission from Ref. [1] (Copyright 2009, Tsinghua University Press).

carrier collection for a given material quality [18]. This design parameter is not available to planar cells since the carrier collection and light absorption directions are parallel. This design parameter enables NPL PV from even moderate quality materials to display excellent carrier collection efficiencies. However, the surface and interface area in NPL PV is significantly enhanced over planar cells. Thus it is critical to choose material systems with low interfacial and surface recombination rates to minimize carrier loss at interfaces. For instance, InP [32], CdS [33] and CdTe [34] exhibit low surface recombination velocities in the range of 10^2-10^4 cm/s. For Si, the recombination velocities of untreated surfaces are reported to be in the range of 10^4-10^7 cm/s, but can be reduced to $\sim 10^2$ cm/s by appropriate surface passivation [35].

Each architecture has its advantages and drawbacks with respect to the control over optical properties and electronic properties as well as ease of fabrication. Embedded NPLs enable maximization of carrier collection by adjusting the NPL pitch, allowing moderate efficiencies to be achieved even if the absorber material has a low bulk minority carrier lifetime. However, due to the planar top surface, the optical properties are similar to planar cells when the thin film is the absorber material. On the other hand, free-standing core-shell NPLs, enable optical engineering of the structure by controlling the size and pitch of the NPLs, as well as the possibility to tune the carrier collection by varying the core-shell radii. This method is more challenging to fabricate, as a conformal coating is needed to form a p-n junction.

While many promising material systems have been explored for thin film solar cells, CdS/CdTe is one of the most prevalent. The advantages of the CdS/CdTe system include the near-ideal bandgap of the CdTe absorber layer, good defect tolerance of poly-CdTe, good quality of the CdS/CdTe hetero-interface, and ease of deposition of this material system. The main limitations are the toxicity of Cd, scarcity of Te, and the lower efficiencies when compared to single-crystalline PV from materials such as Si and GaAs. Regardless, the high quality of the CdS/CdTe interface makes this material system ideal for studying the properties of NPL PV.

Various fabrication approaches have been explored. In one example, to fabricate embedded CdS/CdTe NPL PV cells, a porous anodic aluminum oxide (AAO) was used as a template for nanomaterial growth [28]. In this architecture, the CdTe is the absorber layer, and the CdS NPLs acts as current collectors. Fig. 2 shows a schematic of a CdS/CdTe NPL cell fabrication process. In short, a porous AAO template is fabricated with electroplated Au catalyst seeds for subsequent NPL growth at the bottom of each pore. The CdS pillars are grown via a vapor–liquid–solid (VLS) growth process. The AAO template is etched back, exposing the pillars, and the CdTe absorber layer is then deposited. A semitransparent top contact of copper/gold was then deposited. This process enables the fabrication of an NPL cell on a low-cost metal foil entirely through processes that are compatible with a roll-to-roll fabrication scheme.

To determine the scalability of this fabrication process, a high-throughput roll-to-roll setup was constructed and used to fabricate large scale AAO templates [36]. Fig. 3a shows
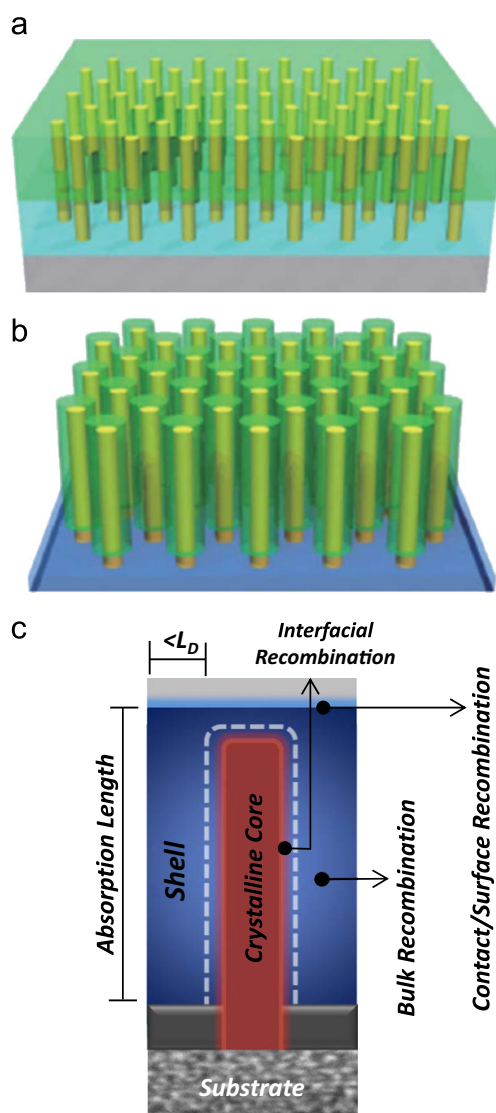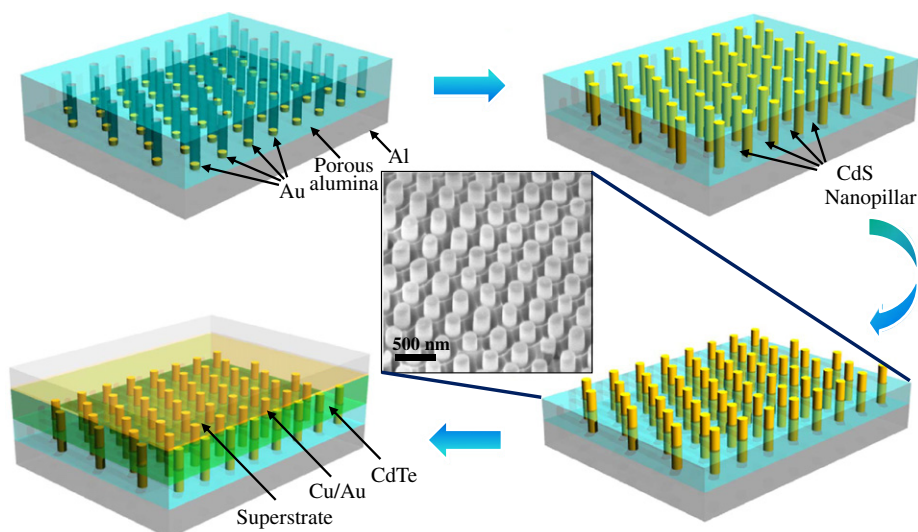
Figure 2 3D solar nanopillar (SNOP) cell fabrication process flow. Reprinted with permission from Ref. [28] (Copyright 2009, Nature Publishing Group).
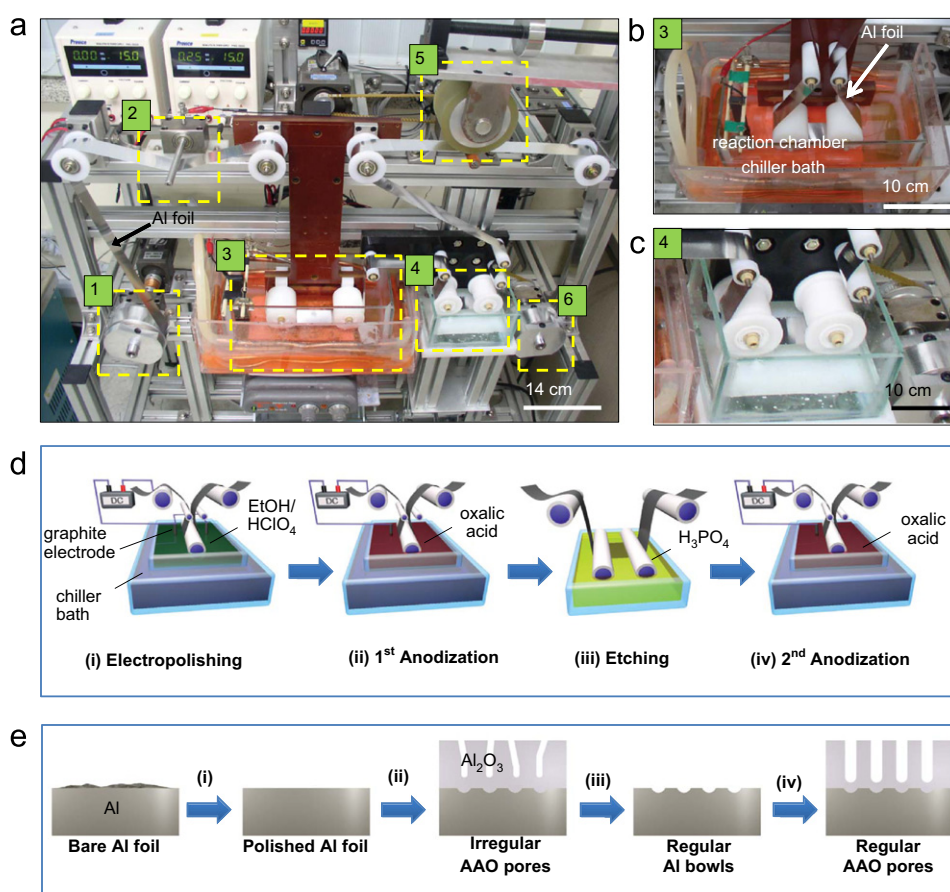

Figure 3 R2R Al texturing system. (a) Optical image of the R2R system used for Al texturization. The important components of the system are highlighted as (1) Al feeding roll, (2) electrical contact to the Al foil, (3) reaction chamber, (4) rinse bath, (5) capstan roll, and (6) rewinding roll. (b) Zoomed-in optical images of the reaction chamber, and (c) the rinse bath, respectively. (d) Schematic diagrams of the process and (e) the resulting surface structure after (i) electropolishing, (ii) first anodization, (iii) AAO wet etching, and (iv) second anodization steps used for the fabrication of various surface textures. Reprinted with permission from Ref. [36] (Copyright 2011, American Chemical Society).

the physical setup used for the roll-to-roll anodization. Specifically, a 3 cm wide roll of 99.5% pure Al foil was used as the stock for the anodization process. The roll is guided via two rollers to a reaction bath held at a constant temperature. The reaction occurs in a solution which is constantly stirred, with the Al foil as the anode, and two graphite rods, arranged symmetrically on either side of the foil as the cathodes. The processing steps required for an AAO template are: (i) electropolishing to smooth the Al surface, (ii) first anodization to texture the Al surface, (iii) removal of the first anodic oxide grown, and (iv) growth of the final anodic oxide, such as that used for templated growth of semiconducting NPLs. A schematic view of the foil configuration in each bath is shown in Fig. 3d, while the resulting Al/AAO structure is shown in the schematic of Fig. 3e. Critically, this process enabled fabrication of large scale (∼10 m in length) AAO. This demonstration clearly illustrates the capability of AAO based NPL PV to be scaled up, a necessity for any PV technology that is to be useful.

One attractive feature of AAO templates is the ability to control the nanoscale structure of each pore through tuning the anodization conditions, and the surface morphology of the initial Al foil [37]. Fig. 4 shows three of the possible pore shapes that can be obtained via pre-texturization of the Al foil. These are achieved by a dual imprint technique utilizing Si gratings prior to anodization; first the grating is pressed into the Al followed by a second imprint that is at a predetermined angle with respect to the first. The variation in pore shape is achieved by varying the angle and pitch of the subsequent imprints. Growth of nanomaterials in AAO provides a promising route towards large area devices that require control of features at the nanoscale.

One of the key advantages of NPL PV over planar cells is the orthogonalization of light absorption and carrier collection directions. This allows a cell to be designed such that it can absorb a majority of the incident photons without sacrificing carrier collection efficiency. In a planar cell, carriers are collected along the same axis that light is absorbed (Fig. 5a), requiring the diffusion length of carriers to be on the order of the absorption length of the material of choice. Since absorption lengths are on the order of microns, efficient planar PV requires high-quality, and often costly materials. On the other hand, minority carrier collection efficiency in NPL PV (Fig. 5b) is independent of

the length, and only a function of NPL pitch. The advantage of independent control of thickness and absorption is evident when looking at a simulation of short circuit current (J_{sc}) vs. pillar pitch for a long bulk minority carrier diffusion length ($L_D = 5\,\mu m$), and a short bulk minority carrier diffusion length ($L_D = 250\,nm$). J_{sc} is directly related to the carrier collection efficiency. The structure shown in Fig. 5c was simulated with all the cell parameters held constant while varying the NPL pitch. As is expected, by reducing the pitch, the J_{sc} of both cells are improved; however, by choosing an appropriate pitch, the carrier collection of the $L_D = 250\,nm$ cell can be almost as high as that of a cell with a bulk diffusion length 20 times higher (Fig. 5d).

While the NPL architecture is excellent at compensating for bulk recombination, the large interfacial and contact areas constrain the choice of material systems that may be used effectively in these architectures [18]. The two metrics of importance when choosing a material system are interfacial recombination, S_i, and the contact recombination, S_c. Fig. 6a–c show the effect of interfacial recombination on the CdS/CdTe cell pictured in Fig. 5c. As the interfacial recombination velocity is increased, the cell with $L_n = 5\,\mu m$ has a drastic reduction in efficiency, while that with a shorter bulk diffusion length is significantly less degraded. The effective carrier lifetime can be expressed as $1/\tau_{eff} = 1/\tau_0 + S_c/L_{n,CdTe} + S_i/W_d$ where W_d is the depletion length and $L_{n,CdTe}$ is the minority carrier diffusion length in CdTe. By comparing the magnitudes of each term, it can be determined which component limits the performance. NPL architectures are useful for material systems where the dominant factor would be $1/\tau_0$, the bulk recombination term. It should be noted that in the simulation results of Fig. 6, a 5 nm thick heavily doped ($N_A = 10^{19}\,cm^{-3}$) p+ layer directly underneath the contacts was used in order to reduce the effect of contact recombination, making the effective $S_c \sim 10^4\,cm/s$. This minority carrier reflector (i.e., the p+ layer) prevents significant carrier loss to the contacts prior to collection, which mainly reduces J_{sc}. This is in contrast to the effect of S_i which reduces mainly V_{oc}.

Besides optimization of the cell electronic properties, the NPL architecture can be engineered to maximize light absorption and minimize reflections [15]. In order to study the effect of NPL diameter on the optical properties, Ge NPL arrays were fabricated in AAO with a fixed pitch of 150 nm
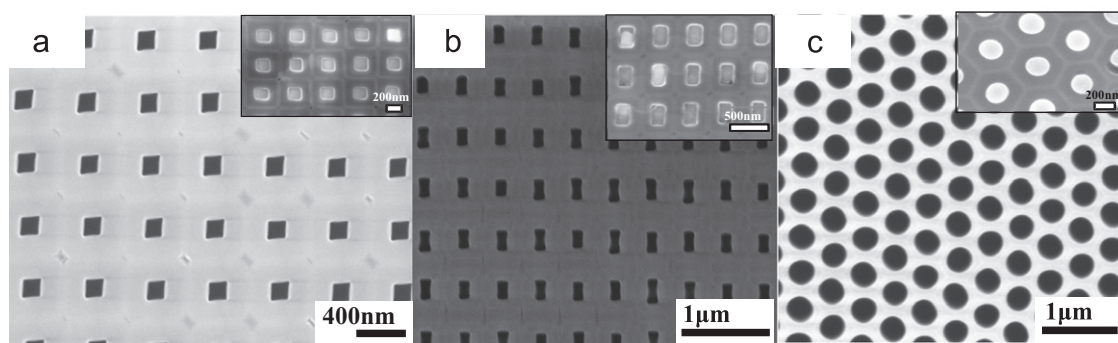

Figure 4 Top-view SEM images of the fabricated AAMs with (a) square, (b) rectangular, and (c) circular pores. Reprinted with permission from Ref. [37] (Copyright 2011, American Chemical Society).
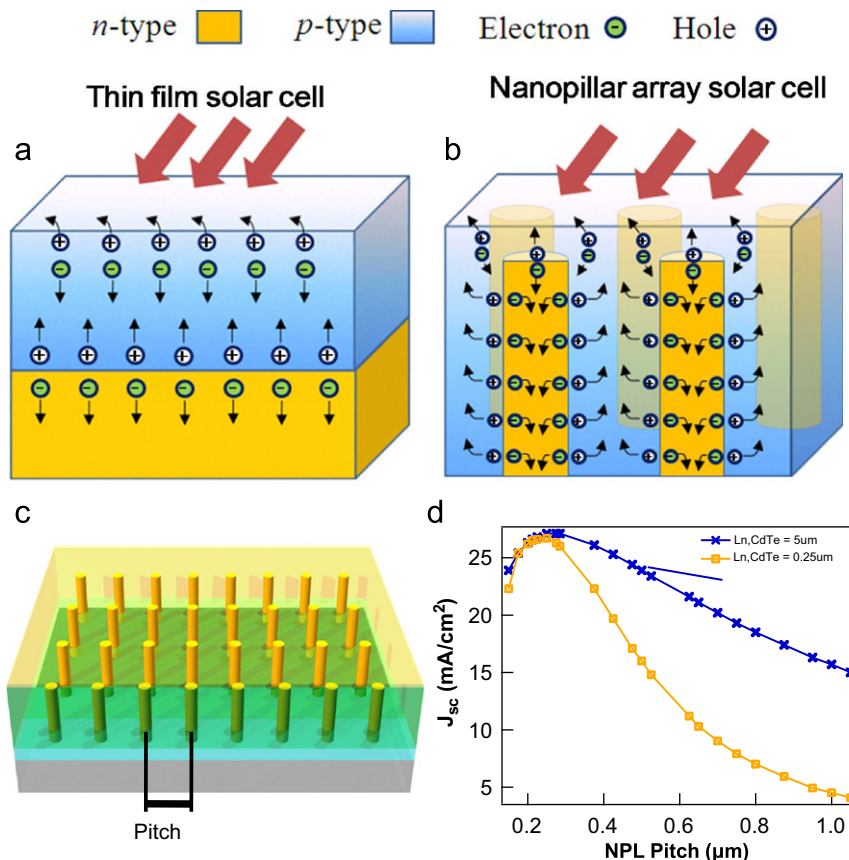
Figure 5 Carrier collection advantages of NPL solar cells. Schematics illustrating charge separation in (a) thin-film solar cells and (b) NPL solar cells. Reprinted with permission from Ref. [28] (Copyright 2009, Nature Publishing Group). (c) Simulation structure used to generate (d) short circuit current as a function of NPL center to center pitch for a fixed NPL diameter for two different minority carrier diffusion lengths. Reprinted with permission from Ref. [18] (Copyright 2010, American Institute of Physics).

and depth of 2 μm. The diameter of the pillars was varied from 60 nm to 130 nm. Fig. 7a shows the effect of NPL diameter on reflectance. As the pillar diameter is reduced, the reflectance is significantly decreased due to the reduction of the fill factor and thus effective index of refraction. However, for a given pillar height, a reduction in the fill factor also reduces the absorption as shown in Fig. 7b. This effect is illustrated in the simulations (Fig. 7b, inset), where the 60 nm pillar (Fig. 7b(B1)) has significantly lower light absorption per unit length than the 130 nm pillar (Fig. 7b(B2)). This is due to the reduced amount of material present. Thus, the overall absorption is a trade-off between the reduction in reflectance and increase in transmittance.

To overcome this limitation, dual-diameter NPLs (DNPLs) can be utilized. The DNPLs are similar to the nanocone structures [38,39] often utilized to reduce reflections. Both structures effectively grade the refractive index in order to reduce the mismatch with air. Fig. 8a and b show a schematic of the array of dual diameter NPLs and a finite-difference-time-domain (FDTD) simulation showing the intensity of the incident light. Fig. 8c shows the SEM images of as-made AAO dual diameter template and the AAO with Ge NPLs grown inside. Most importantly, transmission electron microscopy of the NPL (Fig. 8e1-e4) along

the length shows that it is single crystalline along the entire axis, including the transition region between the two diameters. The transmission and reflection properties of films of these dual diameter NPLs were measured (Fig. 8d), demonstrating that they effectively combine the advantages of both small diameter NPLs and large diameter NPLs. The first generation of CdS/CdTe solar cell utilizing the AAO template (Fig. 9a) yielded promising results, with a power conversion efficiency, η, of ~6%, a short circuit current density, J_{sc}, of ~21 mA/cm², and an open circuit voltage V_{oc} of ~0.6 V (Fig. 9b). These results are particularly promising when considering that the cell had a copper/gold top contact, which was under 70% transparent. These cells compared favorably to the state of the art planar CdS/CdTe cells in terms of current density, which is ~26 mA/cm². However, the V_{oc} is still far below the state of the art ~0.85 V. This may occur due to the low doping concentration of the CdS and CdTe components (i.e., no intentional doping was performed in this work). Additionally, by chemically removing the Al foil and encapsulating the cell in PDMS, a flexible cell could be made. Fig. 9c and d illustrates the effect of bending radius on the J–V characteristics and efficiency. As evident, the characteristics are nearly unaffected by even a small bending radius of 3 cm. Since the NPLs are in the neutral axis of
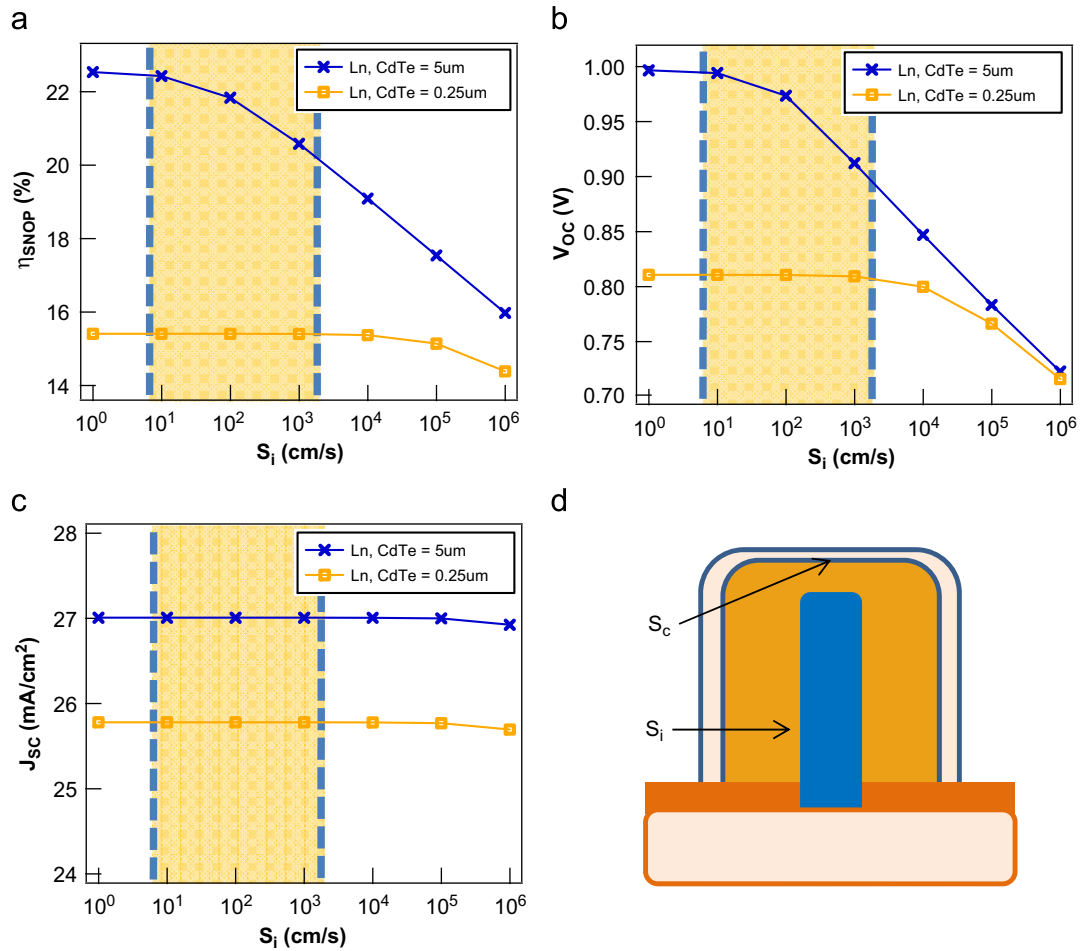
Figure 6 Surface recombination velocity dependency of (a) η, (b) V_{oc}, and (c) J_{sc} are simulated for CdS/CdTe NPL cells with $L_{n,CdTe}$=0.25 and 5 μm. (d) A cross-sectional schematic of the simulated cell is shown. The experimentally reported range for S_i is highlighted for each graph. Reprinted with permission from Ref. [18] (Copyright 2010, American Institute of Physics).
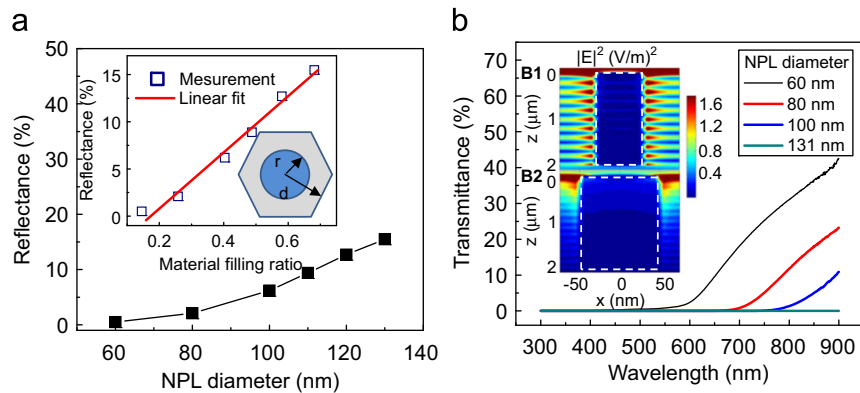

Figure 7 Optical characterization of Ge NPL arrays. (a) NPL diameter dependency of the average reflectance. The inset shows the reflectance dependence on the material filling ratio, FR, defined as the occupation of a NPL cross section area in a hexagonal unit cell of AAO. (b) Experimental transmittance spectra, where insets are the simulated cross-sectional, electric-field intensity $|E|^2$ distribution for a 800 nm wavelength propagating wave in a Ge NPL with a diameter of 60 nm (top) and 100 nm (bottom). Reprinted with permission from Ref. [15]. (Copyright 2010, American Chemical Society).

bending, they experience almost no strain, even for small bending radii. It should be noted that this cell was the first generation, and was unoptimized with respect to multiple

areas, including the top contact transmission, CdS pillar doping, CdS pillar height, and ohmic contacts. However, the cell still demonstrated a respectable J_{sc}=21 mA/cm^2, which
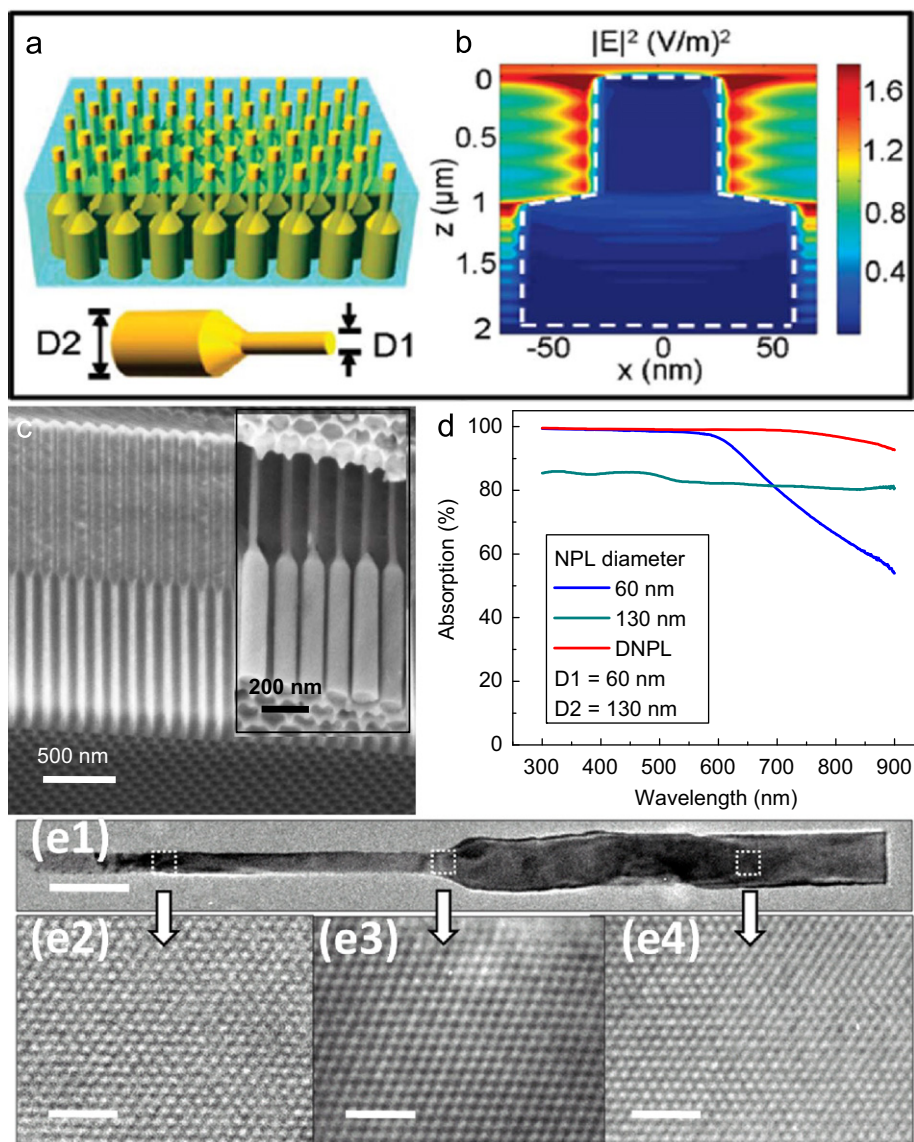
Figure 8 Ge dual-diameter nanopillar arrays. (a) Schematic of a DNPL array embedded in AAM. (b) Simulated cross-sectional electric field intensity distribution for a 800 nm wavelength EM wave propagating in a DNPL with a tip diameter $D1 = 60$ nm and a base diameter $D2 = 130$ nm. (c) Cross-sectional SEM images of a blank AAO with dual-diameter pores and the Ge DNPLs (inset) after the growth. (d) Experimental absorption spectra of dual-diameter NPL-arrays, and single-diameter NPL arrays with diameters of 60 and 130 nm. (e1–e4) TEM images of a Ge dual-diameter NPL, showing the single-crystalline structure along its axis. Reprinted with permission from Ref. [15]. (Copyright 2010, American Chemical Society).

highlights the strength of this architecture in maximizing carrier collection even in poor films.

GaAs is one of the most widely explored III-V for high-efficiency PV. However, the prohibitively high surface recombination velocities for GaAs make it a poor choice for nanostructured cells. Unlike GaAs, InP has excellent surface properties, making it an ideal choice for nanostructured solar cells. Here, both top-down and bottom-up approaches for radial InP homojunction PV are reviewed.

While the AAO templates easily enabled the embedded NPL architecture, due to the small diameter and pitch of the NPLs, fabricating core-shell architecture PV cells are more challenging. In order to realize core-shell homojunction NPL

PV, a highly conformal shell must be either deposited on the core NPL, or a thin, controlled doped layer must be formed. When forming core-shell NPLs, conventional doping techniques fall short. Specifically, gas phase doping does not enable adequate control over dose and uniformity, while ion implantation is highly non-uniform and can induce significant lattice damage. To demonstrate core-shell NPL PV, monolayer doping [40] was used in conjunction with top down etching of a single crystalline InP wafer. Specifically, a Zn doped (2×10^{17} cm^{-3}) p-type InP (1 0 0) wafer was used [41]. To etch the pillars, monodisperse 540 nm silica beads spin-coated on the substrate followed by a two-step reactive-ion etch (RIE) to initially shrink the silica beads
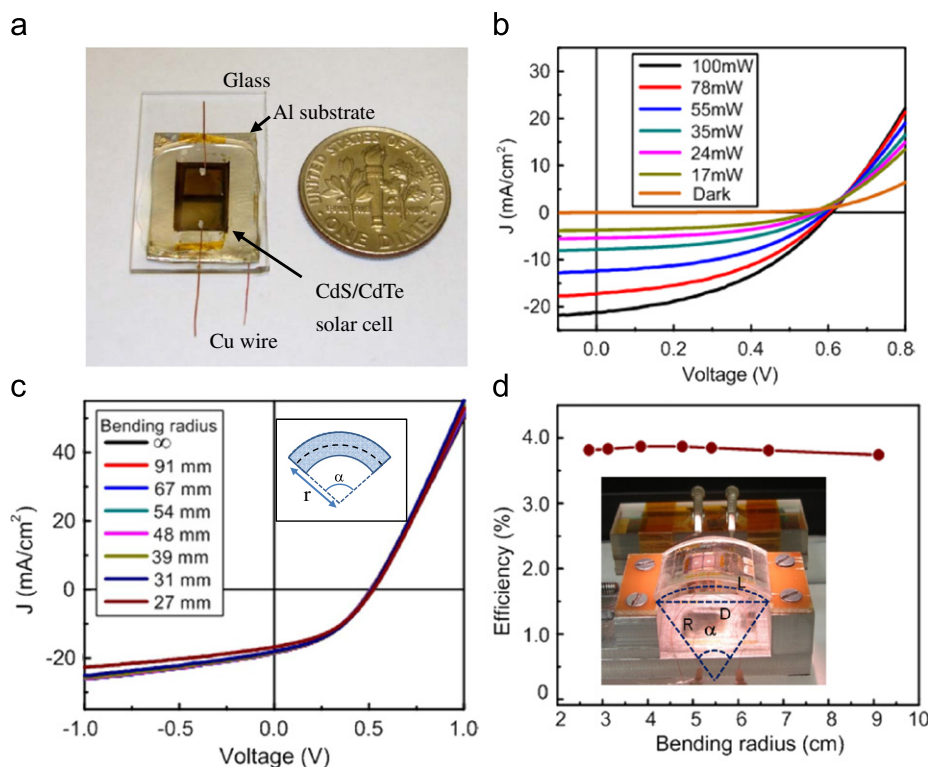
Figure 9 Performance characterization of a representative SNOP cell. (a) An optical image of a fully fabricated SNOP cell bonded on a glass substrate. (b) *I-V* characteristics at different illumination intensities. (c) *I-V* characteristics of a flexible cell for various bending radii. (d) Performance characterization of a flexible SNOP cell, showing minimal change in V_{oc} and η on bending of the substrate. The inset shows a picture of the set-up for bending the flexible modules. Reprinted with permission from Ref. [28]. (Copyright 2009, Nature Publishing Group).

and then etch the InP into NPLs (Fig. 10a). Following RIE, the beads were removed in HF and the surface of the NPLs was cleaned by treatment in HCl solution followed by HNO_3 solution. SEM images of the resulting NPLs are shown in Fig. 11a. The NPL pitch was ~400 nm, reducing the reflection from 30% for the planar InP wafer, to ~5% for the pillars within the 450–800 nm wavelength.

After fabrication of the InP NPLs, a conformal n-type shell was created via monolayer doping, a technique that uses a self-assembled monolayer (SAM) of dopant, followed by a capping and drive-in process to heavily and precisely dope an ultra-shallow junction. Here, the NPLs were placed in an ammonium sulfide solution to create a monolayer of S on the InP surface. After a 100 nm SiO_x capping layer, the S was driven into the NPLs at 570 °C for 15 min (Fig. 10b). The doping concentration on InP after MLD (Fig. 11b) from SIMS is 10^{19}-10^{20}, with a junction depth of ~10 nm (Ref. [41]). After back and top contacts (Fig. 11c) were evaporated onto the InP, the light and dark curves were measured under an AM1.5g spectrum. The cells achieved a respectable power conversion efficiency of 8.1%, with a J_{sc}=25 mA/cm^2 and a V_{oc}=0.54 V. The device performance was limited by the contacts, as well as the surface recombination of the NPLs, which were likely heavily damaged during the RIE process. Specifically, this cell demonstrated a viable route towards core-shell NPLs through the highly-controlled MLD process.

Arrays of InP NPLs fabricated via catalyst free selective-area metalorganic vapor phase epitaxy (MOVPE) have also been used by other groups to fabricate PV cells [42]. Specifically,

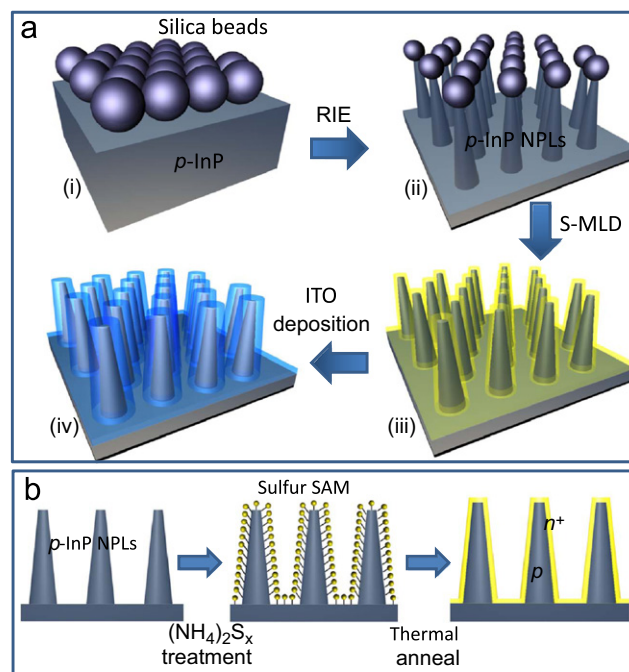**Figure 10** (a) The fabrication process schematic of InP NPL solar cells, involving (i) silica beads (diameter of ~540 nm) assembly on a bulk *p*-InP wafer, (ii) InP RIE and silica beads wet etching, (iii) S-MLD of NPLs, and (iv) sputtering of ITO top contact. (b) Detailed process schematic of the S-MLD process. Reprinted with permission from Ref. [41] (Copyright 2011, American Institute of Physics).
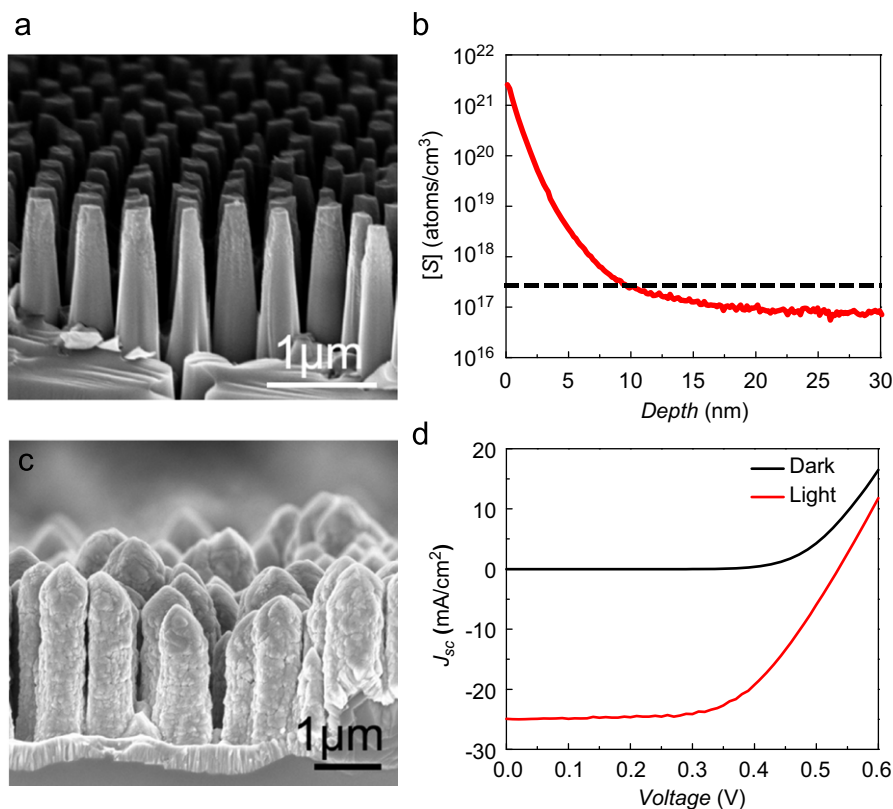
Figure 11 SEM images of (a) as-made NPLs, and (c) NPLs coated with ITO ($\sim$100 nm thick). (b) Sulfur SIMS profile of an InP wafer after the S-MLD process. The dashed line shows the background Zn concentration of 2×10^{17} cm^{-3}. (d) I-V characteristics under dark and AM 1.5G illumination. Reprinted with permission from Ref. [41] (Copyright 2011, American Institute of Physics).

a p-type InP core was grown on the substrate, followed by epitaxial growth of an n-type shell. To selectively grow NPLs, SiO_2 was deposited and patterned on a p-type InP (1 1 1)A wafer. Core NPL growth was carried out at 660 °C using trimethylindium (TMI), and tertiarybutylphosphine (TBP), and diethylzinc (DEZ). The shell growth was achieved by decreasing the growth temperature to 600 °C and using SiH_4 as the dopant precursor. Fig. 12a and b show the as-grown InP cores and the core-shell NPLs, respectively. The cores take on both triangular and hexagonal shapes, while after shell growth, all NPLs have a hexagonal shape. The overall array filling factor was 27%.

Devices were subsequently fabricated by filling the space between the NPLs with CYCLOTENE resin (Dow Chemical) to act as a transparent insulator. The tips of the NPLs were exposed by etching the resin via reactive ion etching. Indium tin oxide was sputtered to make contact to the NPL array. An SEM image of a fully fabricated cell is shown in Fig. 12c. The cells performance (Fig. 12d) under AM1.5G illumination showed an V_{OC} of 0.43 V, J_{SC} of 13.72 mA/cm^2 and a FF of 0.57, giving 3.37% overall efficiency.

Si is an attractive material system for the NPL cell given its dominance in the semiconductor and solar industries. The excellent quality with which Si can be grown enables fabrication of high efficiency modules. Similar to GaAs, however, untreated Si has high surface recombination velocity, requiring careful surface passivation in order to effectively make nanostructured PV. In this regard, the use

of surface oxides and nitrides can drastically reduce the surface recombination velocities. The passivation of Si is a topic that has been extensively studied, and in order to take advantage of the significant advantages of NPL PV, it is necessary to utilize a passivation technique that (i) enables low surface recombination velocities, (ii) is easily deposited, and (iii) is stable over the lifetime of the PV device. Additionally, due to the long absorption length, $\sim$100 μm, high efficiency Si PV requires cell thickness to be of the same order of magnitude. However, by taking advantage of the strong light trapping properties of the NPL architecture, the cell thickness can be reduced by over an order of magnitude.

Using a top-down approach to Si NPL fabrication [31], Garnett et al. studied the light trapping properties of Si NPLs, demonstrating an increase in path length of incident photons by up to 73 times. Additionally, they showed that, for unpassivated Si surfaces, there is a competition between absorption enhancement and increased surface recombination. The NPL arrays were fabricated via dip coating silica beads on Si wafers followed by a deep reactive ion etch (DRIE) etch, resulting NPLs that were 390 nm in diameter (Fig. 13a). A radial p-n junction was then formed via boron diffusion with a junction depth calculated to be about 160 nm. Photolithography with aluminum/palladium sputtering was used to form the top contact. To mimic the effect of very thin Si layers, the substrates used were heavily
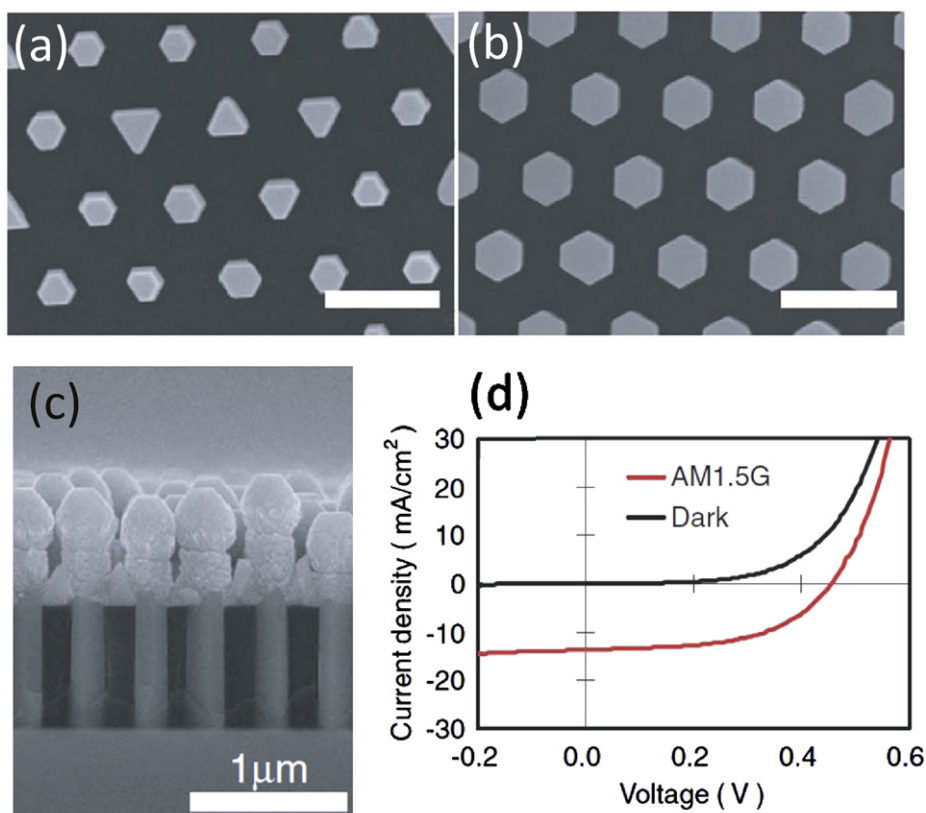
Figure 12 MOCVD grown InP NPLs. (a) SEM image of the top view of the p-type NPL core, (b) the image of the core-shell NPL array, and (c) cross-sectional SEM image of the fabricated device. (d) Measured *I-V* characteristics of a solar cell fabricated with core-shell pn junction NPLs on a p-type InP(1 1 1)A substrate. Reprinted with permission from Ref. [42]. (Copyright 2009, The Japan Society of Applied Physics).

doped Si wafers with lightly doped epitaxial silicon grown on top. Due to the doping dependence of the minority carrier diffusion length this effectively simulates the PV response of thin Si layer without the handling constraints. *I-V* characteristics of 8 μm thick Si with 5 μm NPLs and a planar control cells under dark and AM1.5G illumination conditions are plotted in Fig. 13b. Devices were also fabricated on 20 μm thick Si with and without 5 μm NPLs. For the 20 μm Si film thickness, the average V_{oc} was 0.519 V, J_{sc} was 16.82 mA/cm^2, and overall efficiency was 5.3%. The 8 μm cell was comparable, with V_{oc} of 0.525 V, J_{sc} of 16.45 mA/cm^2, and an efficiency of 4.83%. The similarity in the J_{sc} for both thicknesses indicates that there is a significant light trapping effect from the Si NPLs.

In order to ascertain the effects of the increased surface area, V_{oc}, FF, and J_{sc} of NPL array PV were measured as a function of the roughness factor (RF). This is defined as the actual area divided by the geometric area. From this definition, the RF of a planar cell would be 1. By fixing the cell thickness to 8 μm and then varying the NPL length, the authors show (Fig. 13c and d) that the increase in NPL length both improves light trapping, with improved J_{sc}, and degrade V_{oc} due to enhanced recombination. The effect of the reduced absorber volume was taken into account via the normalized J_{sc}, where the measured J_{sc} was normalized by the fraction of light that should be absorbed compared to a

planar cell. To quantitatively determine the path length enhancement factor (EF) for the cells, the RF was held constant, and the thickness of the cells was increased, enabling extraction of the minimum and maximum EF for each RF. Additionally, from transmission measurements, the EF can be calculated, assuming a coupling efficiency for the incident light into the cell. With a 95% assumption in coupling efficiency, excellent agreement between the two methods of EF extraction is obtained.

While Garnett et al. studied the effect of cells on a single crystalline Si wafer, Putnam et al. have demonstrated PV with conversion efficiencies of up to 7.9% from bottom up Si microwires (μW) [27]. The authors fabricated vertically aligned Si μW (Fig. 14a) on a p++ Si substrate Al$_2$O$_3$ particles dispersed between the μWs to improve light scattering, an Ag back surface reflector to eliminate loss into the substrate, and a-SiN$_x$:H passivation to minimize surface recombination. In addition to utilizing light trapping to reduce the total amount of Si used, the μWs can be embedded in a polymer substrate and peeled off. Fig. 14b shows an SEM image of the film [43], demonstrating the potential of these μW cells to be flexible, in contrast to traditional single crystalline PV.

To fabricate the PV cells, Si μWs were first grown via the VLS growth method; the wires were in-situ doped with BCl$_3$ gas. The as-grown μWs had p-type resistivity of
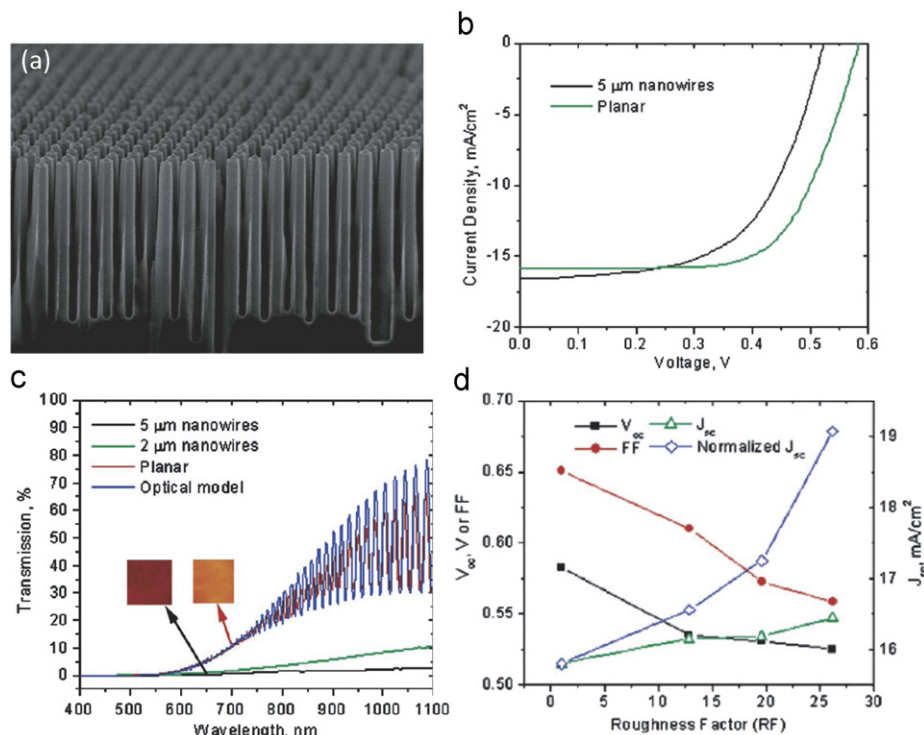
Figure 13 Solar cell fabrication and structure. (a) Tilted cross-sectional SEM of the solar cell. (b) Solar cell output characteristics for a 5 μm NPL and planar control solar cell fabricated from an 8 μm thin silicon absorber. (c) Transmission spectra of thin silicon window structures before (red) and after etching to form 2 μm (green) and 5 μm (black) NPLs. The spectra from an optical model for a 7.5 μm thin silicon window is in blue and matches very well with the planar control measurement. The insets are backlit color images of the membranes before and after etching. Clearly there is a large intensity reduction and red shift in the transmitted light after the NPLs are formed, suggesting strong light trapping. (d) Photovoltaic response and light-trapping effect as a function of roughness factor. The V_{oc}, FF, and J_{sc} of periodic silicon NPL array solar cells fabricated from an 8 μm thick silicon absorber with three different roughness factors (RF) compared to a planar control (RF). The normalized J_{sc} is determined by dividing the NPL J_{sc} by the fraction of light that should be absorbed compared to the planar control, considering the loss in volume for the NPL cells. The increasing J_{sc} with higher RF suggests that the light trapping effect induced by ordered NPL arrays is sufficient to overcome the increased surface and junction recombination that comes with longer NPLs. Reprinted with permission from Ref [31]. (Copyright 2010, American Chemical Society).

$\rho = 0.05\ \Omega\ \mu m$. Radial p-n junctions were then fabricated by thermally oxidizing the entire μW and by partially etching the oxide on the upper portion. Phosphorous was then diffused to a junction depth of ~80 nm to form the junction. Finally, three types of cells were tested, (i) the as-grown cell, (ii) the Scatterer cell with Al_2O_3 particles dispersed between the μWs to scatter light, and (iii) the PRS cell with an additional Ag back coating to prevent loss into the growth substrate, Al_2O_3 scatterers, and an a-SiN$_x$:H passivation layer. Each wire array was then filled to the tips of the wires with a transparent, non-conducting polymer and used ITO as a top contact. Fig. 14a shows the as-grown wires after thermal oxidation and etching, defining the radial p-n junction. The As-Grown cell, the scatterer cell, and PRS cell had wire height distributions of 57-63 μm, 71-78 μm, and 43-49 μm, respectively. Under illumination, the PRS cells significantly outperformed both the Scatterer and the As-Grown cells. The dark (Fig. 14c) and light (Fig. 14d) curves for the champion cells from each category are shown. Importantly, a significant improvement in J_{SC} is shown

between the As-Grown, Scatterer, and PRS cell. This is shown to be due to the improvement in the IQE between the cells, and also reflected in the improvement in J_{SC} between the different cells.

Some of the opportunities and challenges of NPL PV were reviewed. Specifically, the electronic and optical advantages of NPL PV over planar cells provide a strong case for the NPL architectures. There has been much progress on both the design constraints of NPL PV, as well as the fabrication methods for embedded NPL and core-shell NPL PV. The use of AAO for nanomaterial growth as well as MLD for conformal doping of InP NPLs enables NPL PV to be fabricated on a large scale. The constraints of NPL PV are also discussed, focusing on the materials properties required, such as low surface and interfacial recombination velocities. Additionally, work on passivation of both Si μWs and NPLs have shown promising results. Further work is still necessary in integrating all the advances, fabrication, optical, and electronic into one cell that fully exploits the additional degrees of freedom afforded by the NPL architectures.
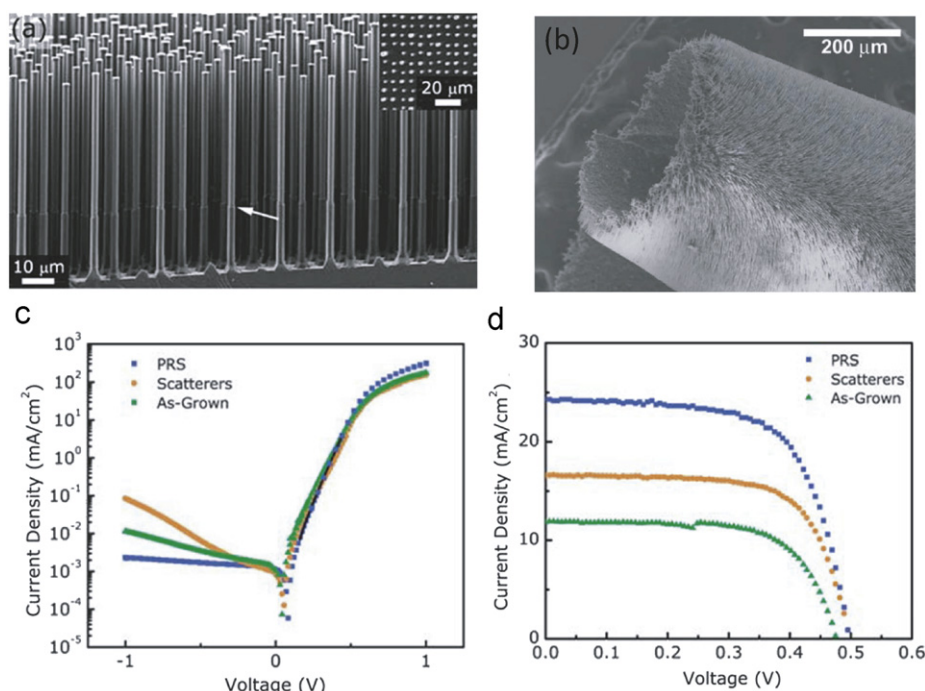
Figure 14 Si microwire array solar cell device geometry. (a) Cross-sectional scanning electron microscope (SEM) image of a Si microwire array after radial p-n junction formation. The white arrow denotes the height of the thermal oxide (used as a phosphorus diffusion barrier in the radial p-n junction fabrication process). Inset: top-down SEM image of the same Si microwire array illustrating the pattern fidelity and slight variation in wire diameter. (b) SEM image of a peeled, polymer-supported wire array demonstrating the flexibility of microwire films. Reprinted with permission from Ref. [43] (Copyright John Wiley & Sons, inc). Current density as a function of voltage for the champion microwire solar cell of each cell type (c) in the dark and (d) under simulated AM 1.5G illumination. The black line in (c) is an exponential fit to the dark J-V data of the PRS solar cell and was used to extract an ideality factor of 1.8. Reprinted with permission from Ref. [27] (Copyright 2011, Royal Society of Chemistry).

References

[1] Z. Fan, D.J. Ruebusch, A.A. Rathore, R. Kapadia, O. Ergen, P.W. Leu, A. Javey, Nano Research (2009) 829.

[2] E.C. Garnett, M.L. Brongersma, Y. Cui, M.D. McGehee, Annual Review of Materials Research (2011) 269.

[3] B. Tian, T.J. Kempa, C.M. Lieber, Chemical Society Reviews 38 (2009) 16.

[4] A.I. Hochbaum, P. Yang, Chemical Reviews 110 (2010) 527.

[5] M. Law, J. Goldberger, P. Yang, Annual Review of Materials Research 34 (2004) 83.

[6] V. Schmidt, J.V. Wittemann, U. Gosele, Chemical Reviews 110 (2010) 361.

[7] H.J. Fan, P. Werner, M. Zacharias, Small 2 (2006) 700.

[8] T. Stelzner, M. Pietsch, G. Andra, F. Falk, E. Ose, S. Christiansen, Nanotechnology 19 (2008) 295203.

[9] K.Q. Peng, Y. Xu, Y. Wu, Y.J. Yan, S.T. Lee, J. Zhu, Small 1 (2005) 1062.

[10] O.L. Muskens, J.G. Rivas, R.E. Algra, E.P.A.M. Bakkers, A. Lagendijk, Nano Letters 8 (2008)2638 8 (2008).

[11] J. Zhu, Z.F. Yu, G.F. Burkhard, C.M. Hsu, S.T. Connor, Y.Q. Xu, Q. Wang, M. McGehee, S.H. Fan, Y. Cui, Nano Letters 9 (2009) 279.

[12] H. Stiebig, N. Senoussaoui, C. Zahren, C. Haase, J. Muller, Progress in Photovoltaics 14 (2006) 13.

[13] L. Tsakalakos, J. Balch, J. Fronheiser, B.A. Korevaar, O. Sulima, J. Rand, Applied Physics Letters 91 (2007) 233117.

[14] Y.B. Tang, Z.H. Chen, H.S. Song, C.S. Lee, H.T. Cong, Nano Letters 8 (2008) 4191.

[15] Z. Fan, R. Kapadia, P.W. Leu, X. Zhang, Y.-L. Chueh, Nano Letters 10 (2010) 3823.

[16] E.D. Kosten, E.L. Warren, H.A. Atwater, Optical Express 19 (2011) 3316.

[17] M.D. Kelzenberg, S.W. Boettcher, J.A. Petykiewicz, D.B. Turner-Evans, M.C. Putnam, E.L. Warren, J.M. Spurgeon, R.M. Briggs, N.S. Lewis, H.A. Atwater, Nature Materials 9 (2010) 239.

[18] R. Kapadia, Z. Fan, A. Javey, Applied Physics Letters 96 (2010) 103116.

[19] B.M. Kayes, H.A. Atwater, N.S. Lewis, Journal of Applied Physics 97 (2005) 1901835.

[20] K.R. Catchpole, S. Mokkapati, F.J. Beck, Journal of Applied Physics (2011) 084519.

[21] A. Wangperawong, S.F. Bent, Applied Physics Letters 98 (2011) 233106.

[22] M.D. Kelzenberg, M.C. Putnam, D.B. Turner-Evans, H.A. Atwater, Predicted efficiency of Si wire array solar cells, in: Proceedings of the 34th IEEE PVSC, 2009.

[23] M.D. Kelzenberg, D.B. Turner-Evans, B.M. Kayes, M.A. Filler, M.C. Putnam, N.S. Lewis, H.A. Atwater, Nano Letters 8 (2008) 710.

[24] M.C. Putnam, D.B. Turner-Evans, M.D. Kelzenberg, S.W. Boettcher, N.S. Lewis, H.A. Atwater, Applied Physics Letters 95 (2009) 163116.

[25] B.Z. Tian, X.L. Zheng, T.J. Kempa, Y. Fang, N.F. Yu, G.H. Yu, J.L. Huang, C.M. Lieber, Nature 449 (2007) 885.

[26] T.J. Kempa, B.Z. Tian, D.R. Kim, J.S. Hu, X.L. Zheng, C.M. Lieber, Nano Letters 8 (2008) 3456.

[27] M.C. Putnam, S.W. Boettcher, M.D. Kelzenberg, D.B. Turner-Evans, J.M. Spurgeon, E.L. Warren, R.M. Briggs, N.S. Lewis, H.A. Atwater, Energy & Environmental Science 3 (2010) 1037.

[28] Z. Fan, H. Razavi, J.W. Do, A. Moriwaki, O. Ergen, Y.-L. Chueh, P.W. Leu, J.C. Ho, T. Takahashi, L.A. Reichertz, S. Neale, K. Yu, M. Wu, J.W. Ager, A. Javey, Nature Materials 8 (2009) 648.

[29] J.A. Czaban, D.A. Thompson, R.R. LaPierre, Nano Letters 9 (2009) 148.

[30] E.C. Garnett, P.D. Yang, Journal of the American Chemical Society 130 (2008) 9224.

[31] E.C. Garnett, P. Yang, Nano Letters 10 (2010) 1082.

[32] C.A. Hoffman, K. Jarasuinas, H.J. Gerritsen, A.V. Nurmikko, Applied Physics Letters 33 (1978) 536.

[33] Y. Rosenwaks, L. Burstein, Y. Shapira, D. Huppert, Applied Physics Letters 57 (1990) 458.

[34] R. Cohen, V. Lyahovitskaya, E. Poles, A. Liu, Y. Rosenwaks, Applied Physics Letters 73 (1998) 1400.

[35] C. Leguijt, P. Lolgen, J.A. Eikelboom, P.H. Amesz, R.A. Steeman, W.C. Sinke, P.M. Sarro, L.A. Verhoef, P.–P. Michiels, Z.H. Chen, A. Rohatgi, Solar Energy Materials and Solar Cells 34 (1994) 177.

[36] M.H. Lee, N. Lim, D.J. Ruebusch, A. Jamshidi, R. Kapadia, R. Lee, T.J. Seok, K. Takei, K.Y. Cho, Z. Fan., H. Jang, M. Wu, G. Cho, A. Javey, Nano Letters 11 (2011) 3425.

[37] O. Ergen, D.J. Ruebusch, H. Fang, A.A. Rathore, R. Kapadia, Z. Fan, K. Takei, A. Jamshidi, M. Wu, A. Javey, Journal of the American Chemical Society 132 (2010) 13972.

[38] Y.-L. Chueh, Z. Fan, K. Takei, H. Ko, R. Kapadia, A.A. Rathore, N. Miller, K. Yu, M. Wu, E.E. Haller, A. Javey, Nano Letters 10 (2010) 520.

[39] J. Zhu, Z. Yu, G.F. Burkhard, C.-M. Hsu, S.T. Connor, Y. Xu, Q. Wang, M. McGehee, S. Fan, Y. Cui., Nano Letters 9 (2009) 279.

[40] J.C. Ho, R. Yerushalmi, Z.A. Jacobson, Z. Fan, R.L. Alley, A. Javey, Nature Materials 7 (2008) 62.

[41] K. Cho, D.J. Ruebusch, M.H. Lee, J.H. Moon, A.C. Ford, R. Kapadia, K. Takei, O. Ergen, A. Javey, Applied Physics Letters 98 (2011) 203101.

[42] H. Goto, K. Nosaki, K. Tomioka, S. Hara, K. Hiruma, J. Motohisa, T. Fukui, Applied Physics Express 2 (2009) 035004.

[43] J.M. Spurgeon, S.W. Boettcher, M.D. Kelzenberg, B.S. Brunschwig, H.A. Atwater, N.S. Lewis, Advanced Materials 22 (2010) 3277.

Rehan Kapadia received his BSEE from The University of Texas at Austin in 2008. He is now pursuing his Ph.D in electrical engineering under Prof. Ali Javey in The University of California, Berkeley, where he received his MSEE in 2010. His research centers on the physics and material science of novel nanoscale electronic devices, including photovoltaics and high mobility transistors. He is the recipient of an NSF graduate research fellowship.

Dr. Zhiyong Fan received his B.S. and M.S. degree in physical electronics from Fudan University, Shanghai, China, in 1998 and 2001. He received Ph.D. degree from University of California, Irvine in 2006 in Materials Science. From 2007 to 2010, he worked in University of California, Berkeley as a postdoctoral fellow in department of Electrical Engineering and Computer Sciences, with a joint appointment with Lawrence Berkeley National Laboratory. In May 2010, he joined Hong Kong University of Science and Technology as an assistant professor. His research interests include engineering novel nanostructures with functional materials, for technological applications including energy conversion, electronics, sensors, etc.

Kuniharu Takei received a Ph.D. degree in electrical engineering from Toyohashi University of Technology in Japan in 2009. During his Ph.D. studies, he was a research fellow of the Japan Society for the Promotion of Science. His Ph.D. research focused on CMOS and MEMS integration for neural electronic interfaces such as spike signal recordings and drug deliveries. He has been a Postdoctoral Fellow at the University of California, Berkeley since 2009. His research interests include nanomaterials integration for high-performance electronics on various user-defined substrates. He was awarded a Netexplorateur of the Year Award (2011) for the development of e-skin at Berkeley.

Ali Javey received a Ph.D. degree in chemistry from Stanford University in 2005, and was a Junior Fellow of the Harvard Society of Fellows from 2005 to 2006. He then joined the faculty of the University of California at Berkeley where he is currently an associate professor of Electrical Engineering and Computer Sciences. He is also a faculty scientist at the Lawrence Berkeley National Laboratory where he serves as the program leader of Electronic Materials (E-Mat). He is an associate editor of ACS Nano. His work focuses on the integration of nanoscale electronic materials for various technological applications, including novel nanoelectronics, flexible circuits and sensors, and energy generation and harvesting. He has received numerous awards, including APEC Science Prize for Innovation, Research and Education (2011); IEEE Nanotechnology Early Career Award (2010); Alfred P. Sloan Fellow (2010); National Academy of Sciences Award for Initiatives in Research (2009); Technology Review TR35 (2009); and NSF Early CAREER Award (2008).